Mid-infrared strong coupling between quasibound states in the continuum and epsilon-near-zero modes in a thin polar dielectric film

Ling Yue,[1] Peng Xie,[1] Shiyu Shen,[1] Qi Ding,[1] Hong Zhang,[1,2] and Wei Wang[1,*]

[1]*College of Physics, Sichuan University, Chengdu 610064, China*

[2]*Key Laboratory of High Energy Density Physics and Technology of Ministry of Education, Sichuan University, Chengdu 610065, China*

(Received 20 March 2024; accepted 19 April 2024; published 2 May 2024)

Epsilon-near-zero (ENZ) materials offer promising candidates for the study of strong light-matter interactions due to their exotic optical properties. Quasibound states in the continuum (QBICs) supported by all-dielectric metasurfaces possess the characteristics of high quality factors with flexible tunability, allowing for significant field enhancement and more degrees of freedom for manipulating light-matter interaction at the nanoscale. Here, we propose a two-dimensional all-dielectric metasurface combined with a thin polar dielectric film, which supports the ENZ mode and the inherent transverse optical (TO) phonon mode. We demonstrate a strong QBIC-ENZ coupling with giant and highly tunable coupling strengths. The proposed metasurface can not only support QBIC modes, but can also excite the ENZ mode in polar dielectric film. With the help of the strong field localization and flexible modulation properties of QBIC, we further realize a selective QBIC-ENZ-TO three-mode strong coupling in the hybrid system, demonstrating a large Rabi splitting over 22.1 meV (178 cm^{-1}) at room temperature, which is four times higher than that of the QBIC-ENZ two-mode coupling. We also demonstrate that the three-mode coupling strength can be easily tuned by varying the thickness of the ENZ thin film, which provides an effective approach for the manipulation of the strong light-matter interaction. The proposed all-dielectric platform exhibits strong coupling strength and flexible design tunability, which is expected to provide a different route for the design of ultracompact optical devices at mid-infrared frequencies.

DOI: 10.1103/PhysRevB.109.205405

I. INTRODUCTION

Epsilon-near-zero (ENZ) materials, featured by their vanishing or near-zero permittivity at a particular wavelength, have attracted much attention as promising candidates for the study of exotic light-matter interactions [1–3]. Near the zero-epsilon wavelength, ENZ materials, such as transparent conducting oxides [4,5], semiconductors [6,7], and phonon-based materials [8,9], can exhibit strong field enhancement, deep subwavelength confinement, large nonlinear optical response, and outstanding electro-optical modulation [10–13]. In particular, thin ENZ films can support optical ENZ modes with extremely strong field enhancements within low mode volumes, which greatly facilitates light-matter interactions in a strong coupling regime [14–17].

Recently the strong coupling of ENZ modes with various optical excitations has been extensively studied, including optical Fabry-Pérot (FP) cavity resonances [18] and plasmon polaritons in plasmonic nanocavities or metasurfaces [19–25]. In such hybrid systems, realization of strong couplings takes the advantage of strong field confinement offered by metallic nanostructures. However, plasmon-based systems are limited by the significant intrinsic ohmic loss of metals, which hinders their practical applicability [26,27].

Dielectric nanostructures are emerging as alternative and promising platforms for the study of strong light-matter interactions [28–31]. In contrast to their metallic counterparts, dielectric nanostructures offer not only lower ohmic losses and less heat generation, but they also facilitate integration into applications requiring complementary metal-oxide-semiconductor (CMOS) compatibility [32,33].

By integrating ENZ thin films with polar dielectrics, strong coupling between ENZ modes and phonon polaritons has been realized in the infrared range by prism excitation for momentum compensation [8]. Photonic gap antennas have been proposed to realize ENZ-based strong light-matter interactions [34]. It is composed of an ENZ film embedded within a high-index dielectric, in which giant electric field enhancements are achieved, resulting in the strong coupling between the ENZ thin film and the photonic modes of the dielectric antenna with large enhancements of the far-field spontaneous emission rate and a unidirectional radiation response.

Dielectric metasurfaces have also been applied to enable strong coupling of ENZ materials with Mie resonances [35,36]. Periodic elements in dielectric metasurfaces not only excite various types of Mie modes, but also offer necessary momentum compensation for launching ENZ modes, which greatly reduce the complexity of the structural design by avoiding the use of bulk prism configuration. However, field confinement around Mie resonance is relatively weak compared to their plasmonic counterparts. Moreover, the electric field is mainly concentrated within the dielectric material with a relatively small modal overlap, which leads to a limited coupling strength [36].

*w.wang@scu.edu.cn

The bound states in the continuum (BICs) based on all-dielectric nanostructures have been shown to attract great attention in recent years, owing to their strongly enhanced near fields and large quality (Q) factor properties [37–40]. First proposed in quantum mechanics, BICs, whose energy is located in off-domain states in the continuum, are leaky modes with infinitely large lifetimes and vanishing resonance widths [38]. By controlling the configuration of the structure or introducing perturbations to break the symmetry, the BICs could easily collapse into quasi-BICs (QBICs) [41,42]. Compared to traditional Mie resonances, QBICs possess high Q factors with flexible tunabilities (shape, size, and asymmetry variations). Moreover, the QBIC resonance is generally associated with the simultaneous excitation of optical modes such as electric, magnetic, and higher-order electric quadrupoles, which provides extra degrees of freedom in designing high-performance photonic devices [43]. Considering the unique characteristics of QBIC modes such as strong field confinement, high Q factors, and flexible tunability, it is expected to show great potential for the study of strong light-matter coupling. Here, we present strong coupling between the ENZ modes and QBIC modes supported by all-dielectric nanostructures.

In this paper, we propose a two-dimensional (2D) all-dielectric metasurface combined with a thin ENZ film to demonstrate strong QBIC-ENZ coupling with giant and highly tunable coupling strength. The ENZ thin film not only supports the ENZ mode but also has its transverse optical (TO) phonon mode inherent as a polar crystal. The proposed metasurface can not only support QBIC modes, but can also excite the ENZ mode in polar dielectric film near the longitudinal optical (LO) phonon frequency. Therefore, taking advantage of the strong field localization and flexible modulation properties of QBIC, we further realize a selective QBIC-ENZ-TO three-mode strong coupling in the hybrid system. A large Rabi splitting up to 22.1 meV is achieved at room temperature, which is four times higher than that of the QBIC-ENZ two-mode coupling. We also demonstrate a flexible control of the coupling strength by varying the thickness of the ENZ thin film, which offers an effective way to manipulate strong light-matter interactions. The proposed all-dielectric platform exhibits flexible design tunability, which is expected to be favorable for the design of ultracompact optical devices at mid-infrared frequencies.

II. RESULTS AND DISCUSSION

A. Strong coupling system

The proposed hybrid system, shown in Fig. 1(a), comprises a 2D all-dielectric metasurface. The metasurface is made up of a square array of Ge elliptical disks on top of a quartz thin film, which is supported by a GaF_2 substrate. Figure 1(b) gives a schematic diagram of the cells of this system with detailed specific structural parameters. We focused on two different scenarios, i.e., the presence and absence of the embedded quartz thin film. First, without the embedded quartz film, the two Ge elliptical pairs in the 2D metasurface cell exhibit an angle of θ relative to their major axes. At $\theta = 0^\circ$, the major axes of the two elliptic pairs are parallel and the structure

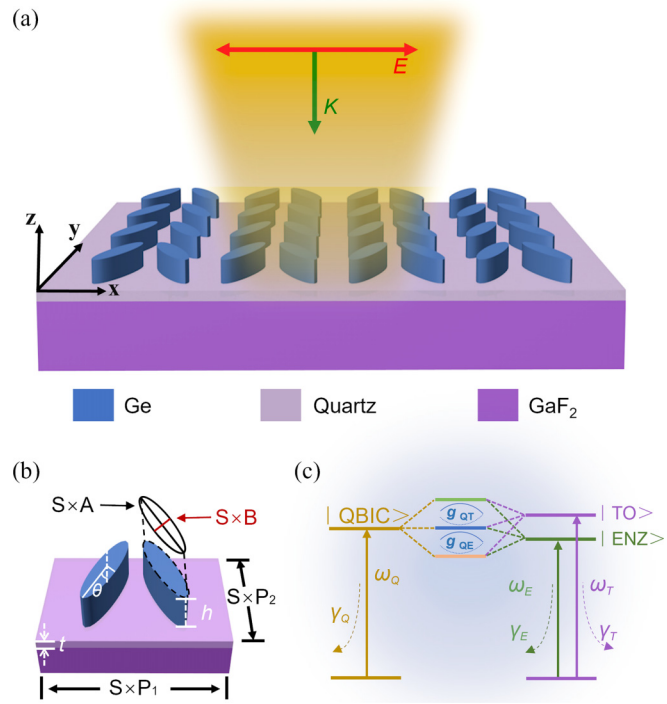

FIG. 1. (a) Three-dimensional schematic of the coupled system, in which the thickness of embedded quartz film is 80 nm. (b) Parametric layout of a single periodic cell: ellipse minor axis B = 1.2 μm, major axis A = 5.2 μm, and periods $P_1 = P_2 = 5.6$ μm; the *S* represents the scaling factor. The center spacing between two Ge disks within one unit cell is 2.8 μm; the height *h* of Ge disks is 0.4 μm. (c) Schematic diagram of the oscillator model of the coupled system.

is in a completely symmetric state, presenting an ideal BIC, which is a leaky mode with infinite Q factor within the continuous background spectrum [39]. When rotation is introduced into the disk pair, i.e., $\theta \neq 0^\circ$, the in-plane symmetry of the structure is broken. The ideal BIC transitions to a finite, but still high Q-factor QBIC resonance, which allows for efficient dynamic tuning of the Q-factor and resonance frequency.

In the presence of a quartz thin film embedded between the 2D metasurface and the GaF_2 substrate, as illustrated in Fig. 1(a), the periodic Ge element can provide additional momentum to compensate for the momentum mismatch between the incident photons and the LO phonon [17]. This results in the excitation of a prominent ENZ mode near its LO phonon frequency ($\omega_{LO} = 1215\ cm^{-1}$) [24], with a substantially enhanced electric field in the thin ENZ film between the two dielectric interlayers. Depending on the vibration direction with respect to the propagation direction, the quartz film also supports a TO phonon mode ($\omega_{TO} = 1072\ cm^{-1}$), which is absent for nonpolar crystals [24,44]. In this sense, three-mode (QBIC, ENZ, and TO phonon) coupling is expected to occur. To better understand the coupling process of the hybrid system, a schematic diagram is given as shown in Fig. 1(c).

In the three-mode coupling system, each mode manifests as the QBIC resonant energy $\hbar\omega_Q$ with decay rate $\hbar\gamma_Q$, the ENZ resonant energy $\hbar\omega_E$ with decay rate $\hbar\gamma_E$, and the TO phonon resonant energy $\hbar\omega_T$ with decay rate $\hbar\gamma_T$, respectively. The mutual coupling strengths of the QBIC-ENZ and

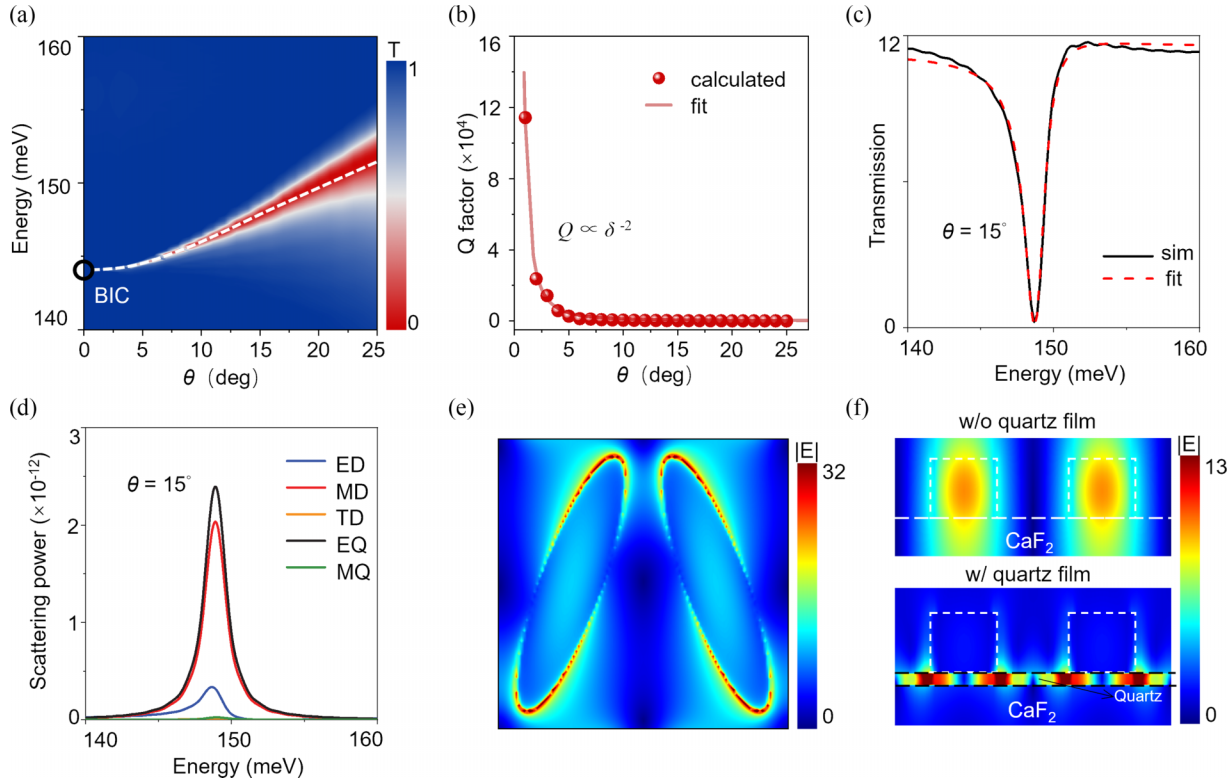

FIG. 2. (a) Transmission color map as a function of titling angle θ and the black circle marks the ideal BIC mode. (b) Red curves and dots represent the fitted and calculated Q factors as a function of θ, respectively. The fitted equation is defined as $\delta = \sin\theta$. (c) Simulating (solid black line) and fitting (dashed red line) the transmission spectra of QBIC mode at $\theta = 15^\circ$. (d) Scattering power of different multipole moments in the unit cell at $\theta = 15^\circ$. ED, MD, TD, EQ, and MQ represent the electric dipole moment, the magnetic dipole moment, the toroidal dipole moment, the electric quadrupole moment, and the magnetic quadrupole moment, respectively. (e) Electric field distribution of the unit cell in the x-y plane at the resonance peak when $\theta = 15^\circ$. (f) Electric field distribution of the unit cell in the x-z plane without and with the quartz film.

the QBIC-TO phonon are denoted by g_{QE}, g_{QT}, respectively. When the coupling between the three modes occurs, the initial energy levels will be significantly changed, leading to the formation of three hybrid states, known as the upper polariton (UP), the middle polariton (MP), and the lower polariton (LP) with a noticeable Rabi splitting in the spectrum. By modulating the resonant wavelength distribution, the anticrossing phenomenon of the eigenvalues can be observed spectrally, exhibiting the typical characteristics of strong coupling.

To quantitatively evaluate the coupling property of the hybrid system, we performed numerical simulations based on the finite difference time domain (FDTD) method. In the simulation process, a TM wave polarized along the x direction is performed to illuminate the structure at normal incidence, as shown in Fig. 1(a). In the x and y directions, periodic boundary conditions are employed, while in the z direction perfectly matched layers (PML) are applied to prevent nonphysical reflections. The permittivity of quartz used in simulations was taken from Refs. [24,45–47] and the refractive indices of GaF_2 and Ge were set to $n_{CaF_2} = 1.38$ and $n_{Ge} = 4.01$, respectively [48].

B. BIC property in 2D Ge disk metasurface

In this section, we first simulated the optical property of the bare 2D metasurface without the quartz film. Here, the dimensions of the elliptical disk were carefully optimized to generate QBIC resonances that can cross over the central wavelength of the ENZ region. Figure 2(a) gives the simulated transmission spectrum of the metasurface as a function of the tilting angle θ. Prominent resonances are visible in the spectra, which gradually shift to higher resonant energy with a broadened linewidth as θ increases from 0° to 25°. This corresponds to a typical transition from ideal BIC (black circle) to QBIC modes as a consequence of the in-plane symmetry breaking. From the simulated transmission spectra, we further extracted the Q factors (denoted by red balls) as a function of θ, as shown in Fig. 2(b). The fitted curve shows an inverse square relationship between the Q factor and the asymmetry parameter δ, which is in agreement with the nature of symmetry-protected BICs [38].

Figure 2(c) gives the simulated transmission spectrum at $\theta = 15^\circ$ (solid black), which exhibits a sharp Fano line shape that can be expressed by a fit to a Fano-type function $T(\omega) = |t(\omega)|^2$ with [49]

$$t(\omega) = a_b + \sum_{j=1}^{N} \frac{b_j \gamma_j e^{i\phi_j}}{\omega - \omega_j + i\gamma_j}. \quad (1)$$

Here a_b, ϕ_j, and b_j are the background amplitude, phase, and amplitude of the transmission spectrum. The fitted spectrum (dashed red) shows excellent agreement with the simulation

result. Therefore, the resonance energy and damping rate of the QBIC mode can be determined to be $\hbar\omega_Q = 149$ meV and $\hbar\Gamma_Q = 2\hbar\gamma_Q = 1.3$ meV, respectively.

We further quantitatively characterized the multipole properties of the QBIC mode by means of the multipole expansion method combined with near-field analysis [41]. As shown in Fig. 2(d), the scattered power of the toroidal dipole (TD), magnetic quadrupole (MQ), and electric dipole (ED) modes are relatively weak compared to the other two modes, i.e., the magnetic dipole (MD) and electric quadrupole (EQ) modes, implying that the EQ and MD modes mainly contribute to QBIC modes. In addition, unlike the Mie resonance where the electric field is primarily localized within the dielectric nanostructures, the simulated near-field results show that the strong field confinement of the QBIC resonance occurs mainly at the edges of Ge elements as shown in Fig. 2(e), with a maximum field enhancement factor of up to 32. Note the part of the electric field is also confined inside the Ge disks, but with a much lower enhancement factor [top panel in Fig. 2(f)]. Such large electric field enhancement at the edges plays a key role in realizing the strong coupling of the QBIC and ENZ modes, as well as the three-mode strong coupling, which will be discussed in later sections.

C. Coupled QBIC-ENZ modes

We now discuss the strong coupling between the QBIC and ENZ modes by introducing a thin quartz film below the 2D metasurface, as shown in Fig. 1(a). For ENZ materials, a general rule of thumb shows that the ENZ mode can exist when its thickness t satisfies the condition $t \leqslant \lambda_{ENZ}/50$ (in our case, $t \leqslant 166$ nm) [14]. To excite an apparent ENZ mode, here we apply the thickness of the quartz film down to $t = 80$ nm, which lies in an ultrathin limit with $d \leqslant \lambda_{ENZ}/100$.

By increasing the tilting angle θ from 10° to 25°, the transmission spectrum (in color scale) of the hybrid nanostructure as a function of θ is shown in Fig. 3(a). A prominent anticrossing behavior is visible, indicating a strong coupling between the QBIC and ENZ modes. To clarify the interaction between these two modes, we extracted the transmission spectrum at zero detuning ($\Delta = \omega_{QBIC} - \omega_{ENZ} = 0$), as shown in Fig. 3(b). Obviously, the strong coupling of the QBIC and ENZ modes leads to the splitting of the fundamental QBIC resonance into two hybrid states, i.e., the lower polariton (LP) branch and the upper polariton (UP) branch. A fitted result (dashed red) to the simulated transmission spectrum by using the Fano-type line shape function [Eq. (1)] is in good agreement with the simulations. By a rough estimation of the energy difference between the UP and LP positions, we identify a considerably large normal mode splitting $\hbar\Omega_{QE} = 5.4$ meV. Such a strong coupling strength actually takes advantage of the unique field distribution in the hybrid system. As shown in Fig. 2(f) (bottom panel), the electric field of the LP branch at zero detuning in the x-z plane is mainly confined within the ENZ layer, which enables a sufficient spatial overlap with the electric field of the BIC mode, thus leading to a greatly enhanced coupling strength.

To quantitatively characterize the coherent coupling between the QBIC and ENZ modes in the hybrid system, we introduce the widely used coupled oscillator model (COM) to

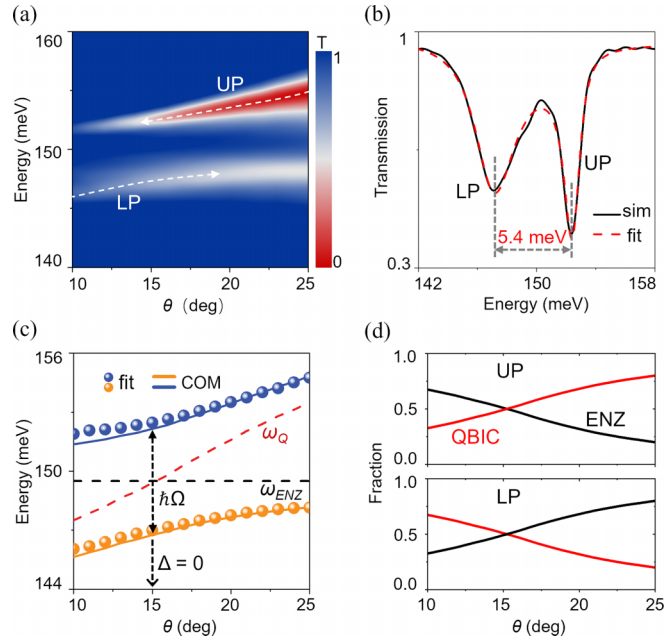

FIG. 3. (a) Transmission spectrum (in color scale) of the QBIC-ENZ hybrid system with titling angle θ ranging from 10° to 25°. (b) Simulating (solid black line) and fitting (dashed red line) the transmission spectra at zero detuning of $\theta = 15°$. (c) The dispersion relationship of the QBIC-ENZ coupling system acquired by the coupled oscillator model (solid lines) as well as by fitting the simulated spectrum (spheres). The black and red dashed lines represent the uncoupled QBIC and ENZ modes, respectively. (d) The QBIC and ENZ fractions in the UP and LP states.

describe the interaction process as follows [50]:

$$\hbar\begin{pmatrix}\omega_Q - i\gamma_Q & g_{QE}\\ g_{QE} & \omega_E - i\gamma_E\end{pmatrix}\begin{pmatrix}\alpha\\ \beta\end{pmatrix} = \hbar\omega_\pm\begin{pmatrix}\alpha\\ \beta\end{pmatrix}, \tag{2}$$

where $\hbar\omega_Q$ and $\hbar\omega_E$ represent the resonance energies of the uncoupled QBIC and ENZ modes, respectively. The coupling strength is denoted by g_{QE}. Additionally, the half widths at half maximum (HWHM) of QBIC and ENZ modes are $\hbar\Gamma_Q = 1.3$ meV and $\hbar\Gamma_E = 1.7$ meV, respectively. α and β are the components of the eigenvectors, which satisfy a relationship of $|\alpha|^2 + |\beta|^2 = 1$. By diagonalizing Eq. (2), the dispersion of hybrid modes can be expressed as

$$E_\pm = \hbar\omega_\pm = \frac{\hbar}{2}\Big[(\omega_Q + \omega_E - i\gamma_E - i\gamma_Q) \pm \sqrt{4g_{QE}^2 + [\omega_Q - \omega_E - i(\gamma_E - \gamma_Q)]^2}\Big]. \tag{3}$$

At zero detuning, i.e., $\omega_Q = \omega_E$, the Rabi splitting can be calculated as

$$g_{QE} = \tfrac{1}{2}\sqrt{\Omega_{QE}^2 + (\gamma_E - \gamma_Q)^2}. \tag{4}$$

The QBIC-ENZ coupling strength is calculated to be $g_{QE} = 2.7$ meV based on Eq. (4). By introducing this coupling strength into Eq. (2), the dispersion relation of hybrid states can be further obtained [solid blue line: UP; solid yellow line: LP; see Fig. 3(c)], well consistent with fitted data (blue sphere: UP; yellow sphere: LP), and the uncoupled QBIC and ENZ resonances are represented by dashed lines as reference.

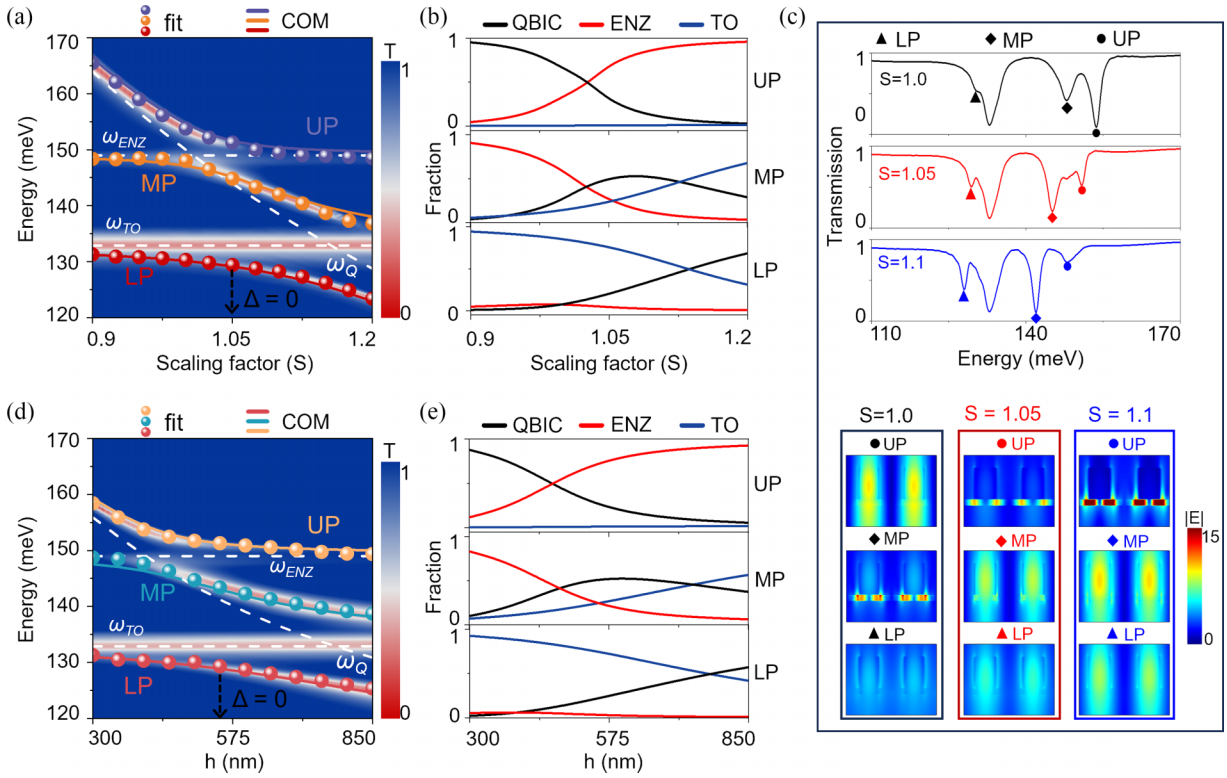

FIG. 4. (a) Transmission spectrum (in color scale) of the QBIC-ENZ-TO hybrid system with scaling factor S. The dispersion relations are obtained by fitting the simulated transmission spectra (spheres) and model (solid lines), respectively. The white dashed lines represent the uncoupled QBIC, ENZ, and TO phonon modes. (b) The QBIC, ENZ, and TO fractions in UP, MP, and LP states with varying scaling factor S. (c) Electromagnetic simulations of the UP-MP-LP mode evolution of the hybrid system. Top panel: transmission spectrum of the QBIC-ENZ-TO hybrid system at scaling factor S of 1.0, 1.05, and 1.1, respectively. Bottom panel: simulated electric field distributions in the x-z plane for UP (circle), MP (diamond), and LP (triangle) at $S = 1.0$, 1.05, and 1.1 (corresponding to the top panel). (d) Transmission spectrum (in color scale) of the QBIC-ENZ-TO hybrid system as a function of the height h of Ge disks. (e) The QBIC, ENZ, and TO fractions in UP, MP, and LP with varying the height h.

To ensure that the hybrid system is in the strongly coupled state, the strong coupling condition should be satisfied, i.e., $g_{QE} > |\gamma_E - \gamma_Q|/2$ and $g_{QE} > \sqrt{(\gamma_E^2 + \gamma_Q^2)/2}$. The former guarantees the existence of Rabi splitting, while the latter ensures that it can be verified experimentally. For the present hybrid system, both conditions are satisfied.

D. Three-mode QBIC-ENZ-TO hybrid system

In the previous section, we have successfully demonstrated the strong coupling between the QBIC mode of the 2D metasurface and the ENZ mode supported by the quartz thin film; however, the coupling strength is relatively limited. Next, we take advantage of the flexible tunability of the QBIC mode so that its resonance can simultaneously cross the resonance energies of the ENZ mode and TO phonon of the quartz thin film, realizing a strong three-mode interaction and further enhancement of the coupling strength.

To realize a three-mode coupling, it is necessary to excite a QBIC mode with a broadband tuning range to cover both the ENZ and the TO phonon resonances. However, the QBIC mode in the previous discussion exhibits a limited tuning range (144–152 meV) when varying the tilting angle θ, as shown in Fig. 2(a). In this section, a different strategy is employed to realize a large tuning of the QBIC mode over a broad spectral range by varying the scaling factor S with fixed $\theta = 15°$. Figure S1(a) in the Supplemental Material [51] gives the transmission spectrum (in color scale) of the QBIC resonance as a function of the scaling factor S. An over 36 meV tuning range (164 to 128 meV) for the QBIC resonance is achieved as the scaling factor S varies from 0.9 to 1.2, which greatly facilitates a sufficient three-mode coupling.

With an embedded quartz film (thickness $t = 80$ nm), we simulated the transmission spectra of the QBIC-ENZ-TO hybrid system as a function of the scaling factor with fixed $\theta = 15°$, as shown in Fig. 4(a). It can be clearly seen that their interaction leads to the formation of three hybrid states, i.e., UP, MP, and LP. By fitting the simulated transmission spectrum with Eq. (1), we plot the dispersion curves of the three hybrid states in Fig. 4(a), which are represented by the blue, orange, and red spheres for the UP, MP, and LP states, respectively. We further employ the COM containing three oscillators to obtain a quantitative description of the hybrid system, which can be expressed as [52,53]

$$\hbar \begin{pmatrix} \omega_Q - i\gamma_Q & g_{QE} & g_{QT} \\ g_{QE} & \omega_E - i\gamma_E & 0 \\ g_{QT} & 0 & \omega_T - i\gamma_T \end{pmatrix} \begin{pmatrix} V_1 \\ V_2 \\ V_3 \end{pmatrix} = \hbar\omega_H \begin{pmatrix} V_1 \\ V_2 \\ V_3 \end{pmatrix}. \tag{5}$$

Here, based on Eq. (5), the coupling strengths of the QBIC-ENZ and the QBIC-TO phonon subsystems are calculated to be $\hbar g_{QE} = 3.6$ meV and $\hbar g_{QT} = 6.9$ meV, respectively. V_1, V_2, and V_3 are the eigenvector components; the corresponding $|V_1|^2$, $|V_2|^2$, and $|V_3|^2$ describe the proportion of the QBIC, ENZ, and TO phonon modes in the hybrid polariton states, which satisfy $|V_1|^2 + |V_2|^2 + |V_3|^2 = 1$. Note that the coupling between the ENZ mode and TO phonon mode is neglected due to their strongly detuned resonances. Analogous to the case of the two-coupled oscillator system, the energy difference between the UP and LP states in the three-coupled oscillator system is defined as the Rabi splitting here. At zero tuning with the scaling factor $S = 1.05$ [dashed black arrow in Fig. 4(a)], the resonance energies of the LP and UP states are about 151.5 meV and 129.4 meV, giving rise to the Rabi splitting of $\hbar\Omega_H = 22.1$ meV.

For a three-oscillator system, the criteria for determining the strong coupling can be denoted as

$$\Omega_H > W_{UP}\Gamma_{UP} + W_{MP}\Gamma_{MP} + W_{LP}\Gamma_{LP}, \tag{6}$$

where W_{UP}, W_{MP}, and W_{LP} represent the weighting coefficients of UP, MP, and LP states in the hybrid system. Γ_{UP}, Γ_{MP}, and Γ_{LP} are the linewidths of the three hybrid states. Therefore, the weight contributions corresponding to each of the three states can be derived as

$$\begin{aligned} W_{UP} &= \Gamma_{UP}/(\Gamma_{UP} + \Gamma_{MP} + \Gamma_{LP}), \\ W_{MP} &= \Gamma_{MP}/(\Gamma_{UP} + \Gamma_{MP} + \Gamma_{LP}), \\ W_{LP} &= \Gamma_{LP}/(\Gamma_{UP} + \Gamma_{MP} + \Gamma_{LP}). \end{aligned} \tag{7}$$

Additionally, the linewidths of the UP, MP, and LP states can be obtained by the fractions of the QBIC, ENZ, and TO phonon modes in the hybrid states [as illustrated in Fig. 4(b)]

$$\begin{aligned} \Gamma_{UP} &= 29.7\%\Gamma_Q + 69.6\%\Gamma_E + 0.7\%\Gamma_T, \\ \Gamma_{MP} &= 50.2\%\Gamma_Q + 26.3\%\Gamma_E + 23.5\%\Gamma_T, \\ \Gamma_{LP} &= 20.0\%\Gamma_Q + 4.2\%\Gamma_E + 75.8\%\Gamma_T. \end{aligned} \tag{8}$$

By substituting Eqs. (7) and (8) into Eq. (6), we can determine the criterion for the strong coupling of QBIC-ENZ-TO phonon modes as follows:

$$\Omega_H > 32.7\%\Gamma_Q + 33.7\%\Gamma_E + 33.6\%\Gamma_T. \tag{9}$$

In our case, we have $\hbar\Gamma_Q = 1.0$ meV, $\hbar\Gamma_E = 1.7$ meV, and $\hbar\Gamma_T = 1.6$ meV. Apparently, the strong coupling criterion is fully satisfied with $\hbar\Omega_H = 22.1$ meV, which is four times larger than that of the two-oscillator (QBIC-ENZ) hybrid system ($\hbar\Omega_{QE} = 5.4$ meV).

To better understand the coupling process of the three-coupled oscillator system, we also calculate the mixing fractions of the three hybrid states based on Eq. (5), as shown in Fig. 4(b). The curves representing the contributions of the QBIC, ENZ, and TO phonon modes are marked by the black, red, and blue solid lines, respectively. Clearly, the UP dominantly contributes to the coupling of QBIC and ENZ modes, while the LP is more related to the coupling of the TO phonon with QBIC modes. As the scaling factor S increases, the UP leaves the QBIC mode and moves towards the ENZ mode, accompanied with the decreased $|V_1|^2$ and increased $|V_2|^2$, whereas the LP gradually proceeds from the TO phonon mode to the QBIC mode, leading to a decrease of $|V_3|^2$ and an increase of $|V_1|^2$. Compared to the UP and LP states, more energy exchange channels are exhibited for the MP state and the relative fractions of the three oscillators are $|V_1|^2 = 0.5$, $|V_2|^2 = 0.26$, and $|V_3|^2 = 0.24$ at $S = 1.05$, reflecting the fact that all three oscillators are strongly involved in the interactions of the hybrid coupled system.

The modal hybridization effect in the coupling process can be further manifested by investigating the evolution of the near-field distribution of the hybrid system. Here, we extract the transmission spectra with scaling factors S of 1.0, 1.05, and 1.1 [top panel in Fig. 4(c)], where the positions of UP, MP, and LP in each spectrum are marked, and the corresponding electric field distributions (in the x-z plane) are presented [Fig. 4(c), bottom panel]. It is noted that, when $S = 1.0$, the electric field in UP is primarily localized inside the elliptical disks. Due to the mutual coupling with the quartz thin film, part of the electric field is also localized within the quartz film and leaks into the substrate. With the increase of S, the electric field in the quartz thin film gradually enhances and then exhibits the strong field localization characteristics of the ENZ mode, which is consistent with the trend of the UP state moving from the QBIC mode to the ENZ mode. For the LP state, within the S from 1.0 to 1.1, the electric field is mainly localized in the interior and edges of the elliptical disks, which is related to the fact that the LP state is mainly contributed by the QBIC and TO phonon modes. The localization of the electric field within disks gradually enhances with increasing S, corresponding to the increasing proportion of QBIC modes. In contrast, the electric field distribution of the MP state shifts from the quartz film to the adjacent medium, exhibiting a strong mixing characteristic of QBIC, ENZ, and TO phonon modes at $S = 1.05$.

In addition to changing the scaling factor to achieve tuning of the QBIC mode over a large spectral range, an alternative way is varying the height h of the Ge disks. In this case, the simulated transmission spectrum of QBIC resonances (without quartz thin film) as a function of h from 300 to 850 nm is shown in Fig. S1(b) in the Supplemental Material [51] (fixed $S = 1$, $\theta = 15^\circ$). Figure 4(d) demonstrates the simulated transmission spectrum (in color scale) of the hybrid system (with quartz thin film) as a function of h, which shows a distinctly strong coupling feature (anticrossing) similar to that in Fig. 4(a). To quantitatively describe the coherent coupling process, similarly, we performed a theoretical COM analysis. A good agreement between the model (solid line) and the fitted results (sphere) is obtained. In addition, when h is 550 nm, the Rabi splitting is determined to be 22.0 meV and the corresponding coupling strengths of g_{QE} and g_{QT} are calculated to be 4.1 meV and 6.8 meV, respectively. Moreover, the strong coupling criterion is satisfied in the current case and the fractions in each of the hybrid states are depicted in Fig. 4(e).

More importantly, the quartz thickness plays a crucial role in determining the coupling property of the hybrid system, which offers an effective approach for the manipulation of the three-mode coupling strength. Under the condition that the thickness of quartz film satisfies the existence of ENZ

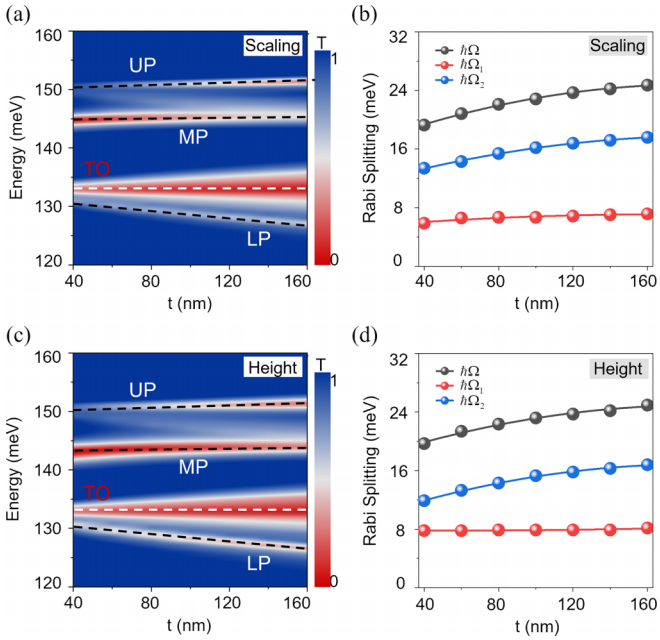

FIG. 5. Panels (a) and (c) are the transmission spectrum of the coupled system at zero detuning as a function of the quartz film thickness (40–160 nm) in the case of adjusting the scaling factor S and the height h of the Ge elliptical disks, respectively. Panels (b) and (d) are the trends of Rabi splitting ($\hbar\Omega$, black curve), UP-MP difference ($\hbar\Omega_1$, red curve), and LP-MP difference ($\hbar\Omega_2$, blue curve) as a function of quartz film thickness for modulating the scaling factor S and varying the height h, respectively.

modes (i.e., $t \leqslant 166$ nm in our case), we first consider the transmission spectrum of the bare quartz film without the 2D metasurface as a function of thickness (see Fig. S2 in the Supplemental Material [51]), which reveals that the enhanced TO phonon mode brings higher transmission spectral peaks and broadened linewidths, implying that more TO phonons are supported with increasing thickness. Next, we further investigate the effect of quartz thickness on the whole hybrid system in two modulation cases (i.e., varying the scaling factor S or the height h of Ge disks).

Figures 5(a) and 5(c) illustrate the simulated transmission spectrum (in color scale) as a function of the quartz thickness t. The variation trend of hybrid states with varying thickness can be clearly observed. Specifically, the LP state exhibits a significant redshift with increasing thickness t, while the UP state is slightly blueshifted. Moreover, the position of the MP state remains almost unchanged. The differences between UP and LP ($\hbar\Omega$, i.e., Rabi splitting) and UP and MP ($\hbar\Omega_1$), as well as LP and MP ($\hbar\Omega_2$) are calculated and represented by black, red, and blue lines, respectively, as shown in Figs. 5(b) and 5(d). It is noted that the Rabi splitting gradually increases with increasing quartz thickness. When the quartz thickness t is 160 nm, the Rabi splitting of the QBIC-ENZ-TO hybrid system increases to 24.7 meV and 24.9 meV in two cases, respectively. In addition, it is also observed that the trend of $\hbar\Omega_2$ is steeper than that of $\hbar\Omega_1$, indicating that $\hbar\Omega_2$ has a greater influence on Rabi splitting with increasing thickness, which may be tightly related to the fact that more TO phonons are involved in the coupling process of the hybrid system, leading to an increase in the coupling strength and a larger Rabi splitting.

III. CONCLUSIONS

In summary, through numerical simulation and theoretical analysis, we systematically demonstrate the QBIC-ENZ two-mode coupling and QBIC-ENZ-TO phonon three-mode strong coupling of the hybrid system by constructing an all-dielectric hybrid nanostructure composed of a highly tunable QBIC resonance metasurface and a quartz thin film. This enriches investigations of the light-matter interaction between QBIC modes and polar dielectrics in the mid-infrared range. Moreover, the coupling strength, energy exchange, and mode evolution are revealed through the coupled harmonic oscillator model together with near-field analysis. Notably, taking advantage of the strong field enhancement of QBIC and ENZ modes, the Rabi splitting of the coupled system is as high as 24.9 meV for the three-mode coupling case, which is four times that of the two-mode coupling. We also find that this three-mode strong coupling could be observed regardless of the regulation of the scaling factor or the height of the Ge disks, which provides more degrees of freedom for manipulating the coupling strength. More importantly, we demonstrate that the thickness of the ENZ film plays a critical role in governing the coupling strength, with further enhancement of the coupling achieved by increasing the quartz thickness to 160 nm. Our findings provide a promising platform for studying light-matter interactions based on all-dielectric nanostructures and open up a different route for the design of mid-infrared nanophotonic devices.

ACKNOWLEDGMENT

This work was supported by the National Natural Science Foundation of China (Grant No. 11974254), Science Specialty Program of Sichuan University (Grant No. 2020SCUNL210).

[1] L. Caspani, R. P. M. Kaipurath, M. Clerici, M. Ferrera, T. Roger, J. Kim, N. Kinsey, M. Pietrzyk, A. Di Falco, V. M. Shalaev, A. Boltasseva, and D. Faccio, Phys. Rev. Lett. **116**, 233901 (2016).

[2] M. Z. Alam, I. D. Leon, and R. W. Boyd, Science **352**, 795 (2016).

[3] X. Niu, X. Hu, S. Chu, and Q. Gong, Adv. Opt. Mater. **6**, 1701292 (2018).

[4] C. Li, X. Tian, G. Yang, S. U. Dev, M. S. Allen, J. W. Allen, and H. Harutyunyan, Phys. Rev. Res. **5**, 013198 (2023).

[5] S. A. Schulz, A. A. Tahir, M. Z. Alam, J. Upham, I. De Leon, and R. W. Boyd, Phys. Rev. A **93**, 063846 (2016).

[6] Y. C. Jun, J. Reno, T. Ribaudo, E. Shaner, J.-J. Greffet, S. Vassant, F. Marquier, M. Sinclair, and I. Brener, Nano Lett. **13**, 5391 (2013).

[7] E. L. Runnerstrom, K. P. Kelley, T. G. Folland, J. R. Nolen, N. Engheta, J. D. Caldwell, and J.-P. Maria, Nano Lett. **19**, 948 (2019).

[8] N. C. Passler, C. R. Gubbin, T. G. Folland, I. Razdolski, D. S. Katzer, D. F. Storm, M. Wolf, S. De Liberato, J. D. Caldwell, and A. Paarmann, Nano Lett. **18**, 4285 (2018).

[9] S. Xu, L. Qian, M. Sun, and G. Zheng, Phys. Chem. Chem. Phys. **25**, 32336 (2023).

[10] M. G. Silveirinha and N. Engheta, Phys. Rev. B **76**, 245109 (2007).

[11] V. Bruno, C. DeVault, S. Vezzoli, Z. Kudyshev, T. Huq, S. Mignuzzi, A. Jacassi, S. Saha, Y. D. Shah, S. A. Maier, D. R. S. Cumming, A. Boltasseva, M. Ferrera, M. Clerici, D. Faccio, R. Sapienza, and V. M. Shalaev, Phys. Rev. Lett. **124**, 043902 (2020).

[12] O. Reshef, I. De Leon, M. Z. Alam, and R. W. Boyd, Nat. Rev. Mater. **4**, 535 (2019).

[13] L. Wen, X. Nan, J. Li, D. R. S. Cumming, X. Hu, and Q. Chen, Opto-Electron. Adv. **5**, 200093 (2022).

[14] S. Campione, I. Brener, and F. Marquier, Phys. Rev. B **91**, 121408(R) (2015).

[15] S. Vassant, J.-P. Hugonin, F. Marquier, and J.-J. Greffet, Opt. Express **20**, 23971 (2012).

[16] S. Vassant, A. Archambault, F. Marquier, F. Pardo, U. Gennser, A. Cavanna, J. L. Pelouard, and J. J. Greffet, Phys. Rev. Lett. **109**, 237401 (2012).

[17] L. Nordin, O. Dominguez, C. M. Roberts, W. Streyer, K. Feng, Z. Fang, V. A. Podolskiy, A. J. Hoffman, and D. Wasserman, Appl. Phys. Lett. **111**, 091105 (2017).

[18] B. Johns, Nanophotonics **12**, 3301 (2023).

[19] S. Choudhary, S. Iqbal, M. Karimi, O. Reshef, M. Z. Alam, and R. W. Boyd, ACS Photon. **10**, 162 (2023).

[20] S. Campione, S. Liu, A. Benz, J. F. Klem, M. B. Sinclair, and I. Brener, Phys. Rev. Appl. **4**, 044011 (2015).

[21] S. Campione, J. R. Wendt, G. A. Keeler, and T. S. Luk, ACS Photon. **3**, 293 (2016).

[22] J. R. Hendrickson, S. Vangala, C. Dass, R. Gibson, J. Goldsmith, K. Leedy, D. E. J. Walker, J. W. Cleary, W. Kim, and J. Guo, ACS Photon. **5**, 776 (2018).

[23] K. Manukyan, M. Z. Alam, C. Liu, K. Pang, H. Song, Z. Zhao, M. Tur, R. W. Boyd, and A. E. Willner, Appl. Phys. Lett. **118**, 241102 (2021).

[24] P. Ma, K. Liu, G. Huang, Y. Ding, W. Du, and T. Wang, Opt. Lett. **47**, 4524 (2022).

[25] B. C. Yildiz and H. Caglayan, Phys. Rev. B **102**, 165303 (2020).

[26] J. B. Khurgin, Nat. Nanotechnol. **10**, 2 (2015).

[27] G. V. Naik, V. M. Shalaev, and A. Boltasseva, Adv. Mater. **25**, 3264 (2013).

[28] S. Y. Shen, Y. Y. Wu, Y. H. Li, P. Xie, Q. Ding, X. Y. Kuang, W. X. Wang, and W. Wang, Phys. Rev. B **105**, 155403 (2022).

[29] K. Sun, M. Sun, Y. Cai, U. Levy, and Z. Han, Nanophotonics **11**, 4221 (2022).

[30] Q. R. Deng, J. F. Chen, L. Long, B. Q. Chen, H. K. Yu, and Z. Y. Li, Opto-Electron. Adv. **5**, 210024 (2022).

[31] P. Xie and Y. Cheng, Phys. Rev. B **108**, 155412 (2023).

[32] A. I. Kuznetsov, A. E. Miroshnichenko, M. L. Brongersma, Y. S. Kivshar, and B. Luk'yanchuk, Science **354**, aag2472 (2016).

[33] R. M. Bakker, D. Permyakov, Y. F. Yu, D. Markovich, R. Paniagua-Dominguez, L. Gonzaga, A. Samusev, Y. Kivshar, B. Luk'yanchuk, and A. I. Kuznetsov, Nano Lett. **15**, 2137 (2015).

[34] A. Patri, K. G. Cognée, D. M. Myers, L. Haeberlé, V. Menon, and S. Kéna-Cohen, Phys. Rev. B **105**, 165126 (2022).

[35] K. Wang, A.-Y. Liu, H.-H. Hsiao, C. Genet, and T. Ebbesen, Nano Lett. **22**, 702 (2022).

[36] M. Karimi, K. M. Awan, Y. Vaddi, R. Alaee, J. Upham, M. Z. Alam, and R. W. Boyd, Nano Lett. **23**, 11555 (2023).

[37] B. Zhen, C. W. Hsu, L. Lu, A. D. Stone, and M. Soljačić, Phys. Rev. Lett. **113**, 257401 (2014).

[38] K. Koshelev, S. Lepeshov, M. Liu, A. Bogdanov, and Y. Kivshar, Phys. Rev. Lett. **121**, 193903 (2018).

[39] C. W. Hsu, B. Zhen, A. D. Stone, J. D. Joannopoulos, and M. Soljacic, Nat. Rev. Mater. **1**, 16048 (2016).

[40] P. L. Hong, L. Xu, and M. Rahmani, Opto-Electron. Adv. **5**, 200097 (2022).

[41] P. Xie, Z. Liang, T. Jia, D. Li, Y. Chen, P. Chang, H. Zhang, and W. Wang, Phys. Rev. B **104**, 125446 (2021).

[42] J. Fan, Z. Li, Z. Xue, H. Xing, D. Lu, G. Xu, J. Gu, J. Han, and L. Cong, Opto-Electron. Sci. **2**, 230006 (2023).

[43] C. Zhou, S. Li, Y. Wang, and M. Zhan, Phys. Rev. B **100**, 195306 (2019).

[44] J. D. Caldwell, L. Lindsay, V. Giannini, I. Vurgaftman, T. L. Reinecke, S. A. Maier, and O. J. Glembocki, Nanophotonics **4**, 44 (2015).

[45] K. Liu, G. Huang, X. Li, G. Zhu, W. Du, and T. Wang, Adv. Mater. **34**, 2109088 (2022).

[46] S. Amarie and F. Keilmann, Phys. Rev. B **83**, 045404 (2011).

[47] P. Li, X. Yang, T. W. W. Mass, J. Hanss, M. Lewin, A.-K. U. Michel, M. Wuttig, and T. Taubner, Nat. Mater. **15**, 870 (2016).

[48] A. Leitis, A. Tittl, M. Liu, B. H. Lee, M. B. Gu, Y. S. Kivshar, and H. Altug, Sci. Adv. **5**, eaaw2871 (2019).

[49] P. Xie, Z. Liang, Z. Li, W. Wang, W. Wang, T. Xu, X. Kuang, L. Qing, D. Li, and J. Yi, Phys. Rev. B **101**, 045403 (2020).

[50] W. Wang, P. Vasa, R. Pomraenke, R. Vogelgesang, A. De Sio, E. Sommer, M. Maiuri, C. Manzoni, G. Cerullo, and C. Lienau, ACS Nano **8**, 1056 (2014).

[51] See Supplemental Material at http://link.aps.org/supplemental/10.1103/PhysRevB.109.205405 for details regarding the influences of scaling factor and the Ge disks height on the QBIC resonance, the dependence of the transmission spectrum of the bare quartz thin layer on its thickness.

[52] P. Xie, Q. Ding, Z. Liang, S. Shen, L. Yue, H. Zhang, and W. Wang, Phys. Rev. B **107**, 075415 (2023).

[53] F. Deng, H. Huang, J.-D. Chen, S. Liu, H. Pang, X. He, and S. Lan, Nano Lett. **22**, 220 (2022).